Aalborg Universitet

AALBORG UNIVERSITY

Dual-band Structure Reused Antenna Based on Quasi-Elliptic Bandpass Frequency Selective Surface for 5G Applications

Zhang, Jin; Zhang, Shuai; Pedersen, Gert Frølund

Communication

Dual-band Structure Reused Antenna Based on Quasi-Elliptic Bandpass Frequency Selective Surface for 5G Applications

Jin Zhang, Shuai Zhang, *Senior Member, IEEE*, and Gert Frølund Pedersen, *Senior Member, IEEE*

Abstract—A dual-band structure reused antenna with quasi-elliptic bandpass feature is proposed in this paper. The antenna consists of a cavity-backed slot array working at K-band (24.2-26.1 GHz) and a frequency selective surface (FSS), which is transparent to the K-band radiation and also reused as a radiator at S-band (2.5-2.7 GHz). The FSS unit cells are designed based on cross-slot structure. By introducing asymmetric boundaries to each unit cell, the FSS obtains high frequency selectivity with two transmission zeros located on each side of the passband. The proposed antenna is fabricated and measured. The measurements have a good matching with the simulations.

Index Terms—Structure Reused Antenna, Metasurface, 5G antennas

I. INTRODUCTION

The upcoming 5th generation (5G) communication requires several frequency bands in a wide range from the microwave to millimeter wave (mm-wave). A compact design of basestations will be a challenge of covering dual frequency range with large frequency ratio (FR). Shared aperture antennas (SAAs) including structure reused antennas (SRAs), which combine the low and high frequency radiators together, will be possible solutions. Dual-band or multi-band SAAs are widely used for radar and satellite applications [1]–[3], where the FR usually ranges from 1.5 to 5.6. Different array elements are accommodated by inserting the high frequency array elements between the low frequency elements. Though some elements are shaped in order to reduce mutual coupling with the adjacent elements, all of them still have to be size reduced in order to keep the element separation close to half wavelength of each center frequency.

Instead of expanding all the elements on one surface, stacking up the elements increases the aperture efficiency. In order to avoid the shadowing, the lower frequency cavity antennas are stacked above the higher frequency cavities, while the lower frequency patches are stacked below the higher frequency patches [4], [5]. This method is suitable for both low and high FR applications but it is difficult to design the feeding networks in a stacked structure.

Dual-band SAA can be realized by exciting different resonating modes on the same aperture [6], [7], where FR is determined by the geometry of the radiator. For some large FR applications, part of the low frequency antenna can be separated and used as high frequency radiator and the performance of the low frequency antenna will not be much influenced [8]–[10]. However, the impedance matching and bandwidth have to be compromised due to the same profile for both bands. An SRA is proposed in [11], in which the antenna reaches a high ratio of aperture reuse (RAR) with high FR. However, the feeding is complicated in fabrication and also the bandwidth of the lower band is very narrow.

Even so, the concept of reusing antenna apertures or structures shows advantages for the high FR dual-band SAA design due to the compact size and high RAR. Based on this, some improvements can
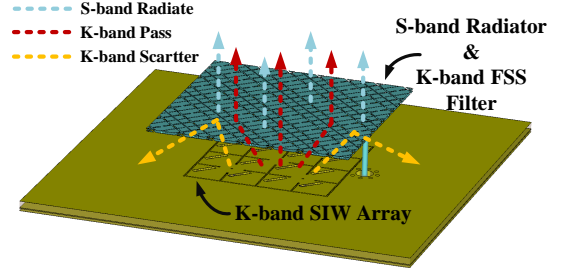
Fig. 1: Schematic of the proposed dual-band SRA.

be made. First, the antenna of each band can be designed individually. The performances of one band do not need to be sacrificed for fitting the requirements of the other band. Second, the concept can still be extended to include some other features, such as filtering, bandwidth increasing, or gain improvement.

In this paper, a dual-band SRA is proposed for 5G basestation applications. The main advantage of this design is that the S-band radiator provides a high selective filtering feature to the K-band radiation, which improves the suppression of the out-of-band emission. The 25 GHz radiation is realized by a 4×4 cavity-backed slot array and the 2.6 GHz radiator is realized by a patch antenna stacked on top of the slot array. In order to let the 25 GHz signal pass through, the patch is modified into a 25 GHz frequency selective surface (FSS), which has a wide passband and high frequency selectivity at 25 GHz. The air gap below the FSS naturally ensures the bandwidth at 2.6 GHz. The 2.6 GHz antenna and 25 GHz array are fed through an SMA and an MMPX connector on the bottom, respectively. The performance of the two bands can be optimized individually, which makes the proposed antenna easily to be modified for applications with different bands and filtering features. The paper is organized as follows: Section II introduces the design of the FSS; Section III presents the performances of the proposed SRA; Section IV provides the measurements and results; and the conclusions are drawn in Section V.

II. DESIGN OF FSS

The concept of the proposed antenna is shown in Fig.1. A K-band bandpass FSS is placed above the slot array, which allows the K-band signal to penetrate. At the same time, the FSS is also shaped to be an S-band radiator, which works similarly to a patch antenna. Therefore, the FSS requires a connected metal surface in order to support the S-band resonating.

Moreover, a fast decay in the stopband is also important for reducing the emission outside the working band. In [12]–[14], multiple transmission zeros are introduced in the FSS in order to achieve a good selectivity. However, the unit cells can not be reused as low frequency radiators due to the 3-dimensions (3D) structures and noncontinuous surface. The FSS with unit cells based on slots can provide a connected metal surface but an FSS with an one-layer substrate can only achieve one transmission zero and thus a
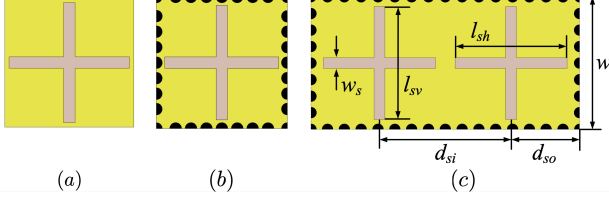
(a)

(b)

Fig. 2: FSS element topology. (a) Conventional cross-slot element. (b) SIW based cross-slot element. (c) Proposed cross-slot element based on larger SIW cavity. (w = 4.9 mm, d_{si} = 4.88 mm, d_{so} = 2.44 mm, w_s = 0.4 mm, l_{sh} = 4.16 mm, l_{sv} = 4.18 mm)
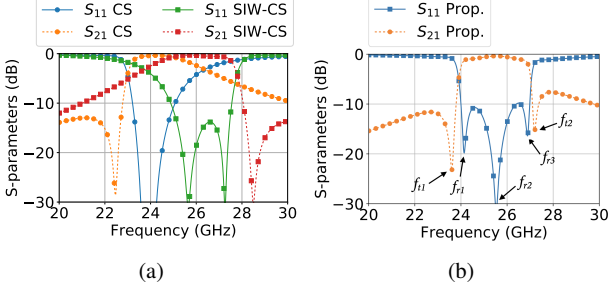

(a)

(b)

Fig. 3: Frequency response of conventional and proposed FSS element topologies. (a) Cross-slot element and SIW based cross-slot element. (b) Proposed cross-slot element with larger SIW.
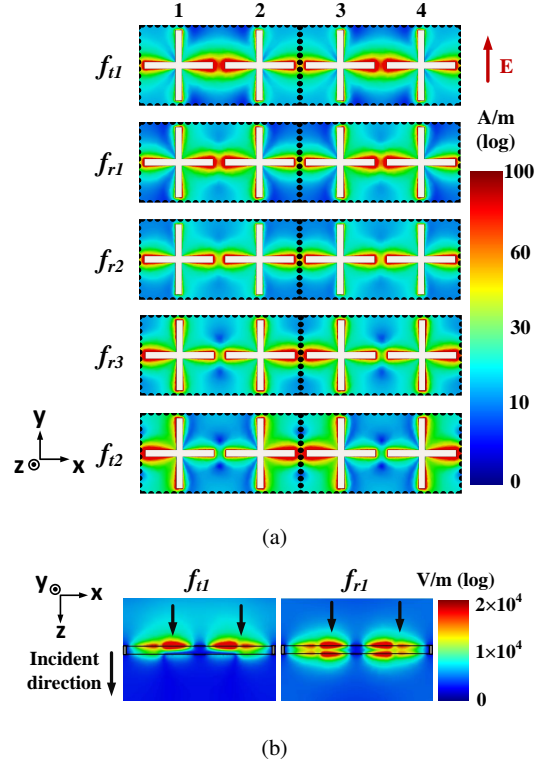
Fig. 4: Average surface current and electric field distribution at transmission and reflection zeros (f_{t1} = 23.62 GHz, f_{r1} = 24.15 GHz, f_{r2} = 25.57 GHz, f_{r3} = 26.91 GHz, f_{t2} = 27.22 GHz). (a) Surface current (the red arrow shows the polarization of electric field of the incident wave). (b) Electric field (the black arrow shows the direction of the incident wave).

slow roll-off is observed on one side of the stopband [15]. Though two transmission zeros can be obtained on multi-layer PCB, the bandwidth is still a limitation [16], [17].

To satisfy the requirements of both K-band filtering and S-band resonating, a combination of cross-slot elements and substrate integrated waveguide (SIW) based cross-slot elements is proposed. The substrate with dielectric constant of 3.66 and thickness of 0.5 mm is used as supporting material. Fig.2(a) shows a conventional cross-slot element. The slots are etched identically on both sides of the substrate. Fig.2(b) shows a cross-slot element based on SIW technology, which has the same size as the structure in Fig.2(a). The frequency response of the cross-slot and the SIW cross-slot FSS are shown in Fig.3(a). The cross-slot FSS has one transmission zero in the lower stopband but a slow roll-off in the higher stopband, while the SIW cross-slot FSS has a transmission zero in the higher stopband and slow roll-off in the lower stopband. The proposed FSS element is shown in Fig.2(c), in which the SIW cavity is enlarged to contain two cross-slot elements on each side. The frequency response of the proposed FSS element is shown in Fig.3(b), which has two transmission zeros located at higher and lower stopband. A rapid roll-off is achieved on both sides of the passband and the bandwidth is also extended.

The resonances in both cross-slot and SIW based cross-slot can be supported due to the asymmetric boundary of each cross. Fig.4(a) shows the average surface current distribution of the transmission and reflection zeros on the two adjacent FSS elements. The red arrow shows the polarization of the incident wave. A strong current is observed between slot 1,2 and 3,4 of the first transmission zero f_{t1} and the first reflection zero f_{r1}. It indicates that f_{t1} and f_{r1} are generated by the coupling of slot 1 and 2, which is similar to the working mechanism of the cross-slot structure. The current distribution is balanced on the two ends of each slot of the second reflection zero f_{r2}, which is, therefore, generated by the resonance of the horizontal slot. For the third reflection zero f_{r3} and the second transmission zero f_{t2}, the current between slot 2 and 3 is stronger. It

means that they are generated by the coupling between slot 2 and 3, which is similar to the working mechanism in the SIW based cross-slot structure.

The working mechanisms between the transmission and the reflection zeros f_{t1} and f_{r1}, as well as f_{r3} and f_{t2}, are different, in spite of the similar surface current distributions. As an example, average electric field distributions on the side view of the FSS at f_{t1} and f_{r1} are illustrated in Fig.4(b). The black arrows indicate the direction of the incident wave. The E-field is stronger on the incidence side at f_{t1}, which means that the incident wave is reflected, and it is at the same level on both sides of the FSS at f_{r1} indicating that the incident wave penetrates the FSS.

Based on the analysis above, we can conclude that: the location of f_{r2} is only determined by the length of the horizontal slots; the locations of f_{r1} and f_{t1} are related and determined by the distance between slot 1 and 2; and the locations of f_{r3} and f_{t2} are related and determined by the distance between slot 2 and 3. Fig.5 shows the locations of the transmission and reflection zeros with different value of d_{si} and d_{so}. d_{si} is the distance between slots 1 and 2 and d_{so} is half the distance between slot 2 and 3. As one of them changes, the other one remains the same. The different d_{si} only influences f_{r1} and f_{t1}, as shown in Fig.5(a), while the different d_{so} only influences f_{r3} and f_{t2}, as shown in Fig.5(b). A wider transmission bandwidth is obtained by placing the transmission zeros more separately but the reflection between the transmission zeros also increases. Therefore, the bandwidth is limited by the requirement of the highest reflection in the passband. In this case, the largest -10-dB reflection bandwidth is reached when f_{r1} is 24.1 GHz and f_{r3} is 26.9 GHz.
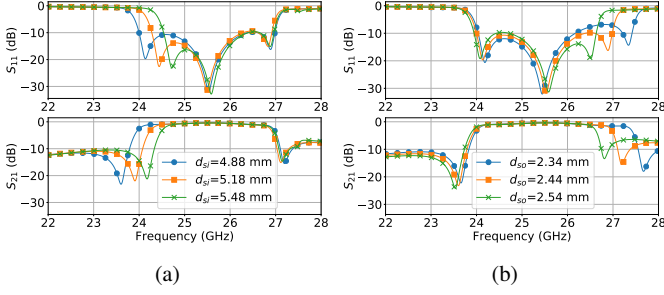
Fig. 5: Locations of transmission poles and zeros with different slot separations. (a) Different separation between slot 1 and 2 (d_{si}). (b) Different separation between slot 2 and 3 (d_{so}).

TABLE I
COMPARISON BETWEEN THE PROPOSED FSS AND OTHER DESIGNS

Ref No.	Zeros	Roll-off Factor k	Layers of Substrates	-10-dB Bandwidth	Aperture Reuse
[14]	2	1.36	3D	4.6%	No
[16]	2	1.7	2	6.2%	No
[12]	2	1.27	3D	11%	No
[13]	3	1.12	2	15.2%	No
[15]	1	1.737	1	25%	Yes
This work	2	1.1	1	11.7%	Yes

Table I shows the comparison between the proposed FSS and the other bandpass FSS designs. The roll-off factor k is calculated by $BW_{(3dB)}/BW_{(10dB)}$, where $BW_{(3dB)}$ and $BW_{(10dB)}$ are the -3-dB and -10-dB bandwidth, respectively. The lower k means better frequency selectivity. The value of k is closer to 1, the FSS is closer to a perfect filter. The proposed FSS achieves k of 1.1, which is the lowest compared with the previous designs. The design in [13] has similar k and higher bandwidth but it is constructed by 3D metal cylindrical pipes and disks, which cannot be reused as a low frequency radiator. The design in [15] is suitable for aperture reusing but it has only one transmission zero and a slow roll-off on one side of the passband.

III. PERFORMANCES OF SRA

The design procedures of cavity-backed slot array and its feeding network can be found in [18]. Fig.6(a) shows the 4×4 slot array, which is constructed by a two-layer stacked PCB. The supporting material has a dielectric constant of 2.2. The radiating slots and the back cavities are on the first layer with a thickness of 1.524 mm. The array is fed by an SIW power divider and a coaxial port (Port 1) on the bottom layer, which is 0.508 mm thick. The detailed dimensions of the top and bottom layers are shown in Fig.6(b) and (c).

The FSS installed on top of the slot array is shown in Fig.7. The height of the air gap is 9.5 mm, which is $0.79\lambda_0$ of 25 GHz and $0.082\lambda_0$ of 2.6 GHz. The FSS has a square shape and the width is 47 mm ($0.41\lambda_0$ of 2.6 GHz). The polarization of the S- and K-band antennas are shown in Fig.7(a), which has a 45° difference. The unit cells are oriented along the diagonal direction in order to match the polarization of the incident wave. The S-band FSS-patch is excited directly by a coaxial port (Port 2).

The average surface current distribution of different frequencies are shown in Fig.8. The current is stronger at the edges of the FSS-patch at 2.6 GHz, when excited from Port 2, as shown in Fig.8(a). It is similar to a patch antenna resonating mode. Fig.8(b) shows the
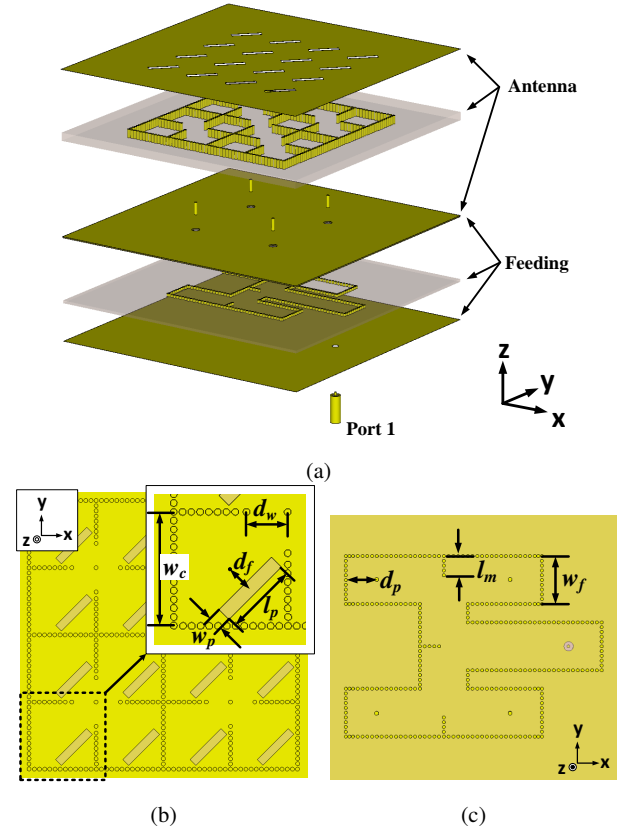

(a)

(b)   (c)

Fig. 6: Cavity-backed slot array at 25 GHz. (a) Exproded view. (b) Top view of the antenna layer. (c) Top view of the feeding layer. (h_1 = 1.524 mm, h_2 = 0.508 mm, w_c = 8.1 mm, w_p = 1 mm, l_p = 5.2 mm, d_f = 1.9 mm, d_w = 3.2 mm, w_f = 6 mm, l_m = 2.4 mm, d_p = 4 mm)

current distribution at 25.5 GHz excited from Port 1, which represents the distribution in the FSS passband. Different from that at 2.6 GHz, the current is concentrated in the center of the patch. The different distributions guarantee a low ports coupling at K-band. It is naturally below -80 dB at S-band due to the cut-off frequency of the feeding SIW at 13.7 GHz. The current distributions in the FSS stopband (23.6 GHz and 27.2 GHz) are shown in Fig.8(c) and Fig.8(d). Both frequencies have lower current on the FSS comparing with that at 25.5 GHz. At 23.6 GHz, the current distribution on the ground plane has higher magnitude than that at the other frequencies, which means that the radiation is scattered to many other directions.

Fig.9 shows the simulated S-parameters and realized gain in the broadside (+z) direction in the two operating bands. Fig.9(a) shows the results at S-band. "FSS-patch" represents the proposed antenna fed from Port 2; "Conv. Patch" represents a square patch antenna with the same size as the FSS-Patch; "w/o SIW SA" represents the proposed FSS-Patch excited alone without the SIW array mounted below. The impedance matching and realized gain turn out to be very similar in all these three occasions. The FSS unit cells only cause a small frequency shift to the lower band and the existence of the K-band SIW slot array has little influence on the S-band radiation. The simulated -10-dB bandwidth of the FSS-Patch antenna is 7.3% from 2.5 GHz to 2.69 GHz. The simulated realized gain ranges from 8.3 dBi to 8.7 dBi.

The simulated gain and reflection performance of the K-band slot array with and without FSS is shown in Fig.9(b). The array has the
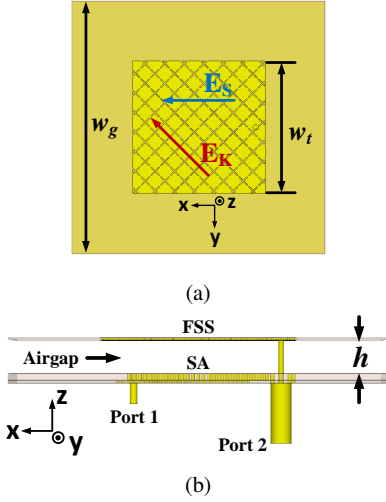
(a)

(b)

Fig. 7: K-band slot array with FSS (FSS-SA). (a) Top view. (b) Side view. (w_g = 90 mm, w_t = 47 mm, h = 9.5 mm)
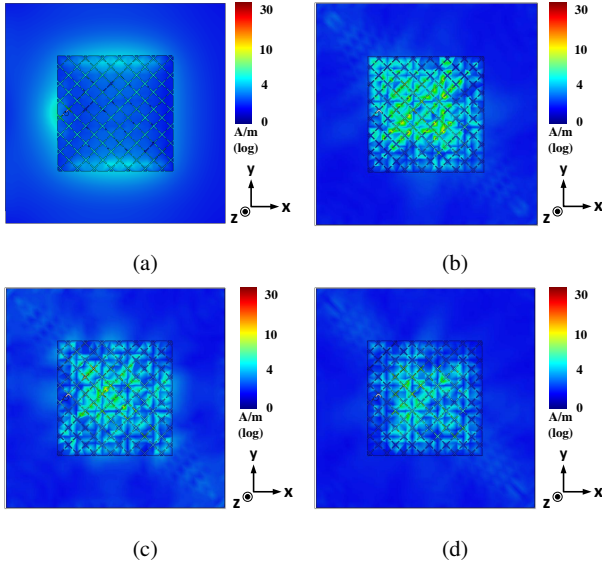

(a)   (b)

(c)   (d)

Fig. 8: Averaged surface current distribution at (a) 2.6 GHz when Port 2 is excited, (b) 25.5 GHz when Port 1 is excited, (c) 23.6 GHz when Port 1 is excited, and (d) 27.2 GHz when Port 1 is excited.
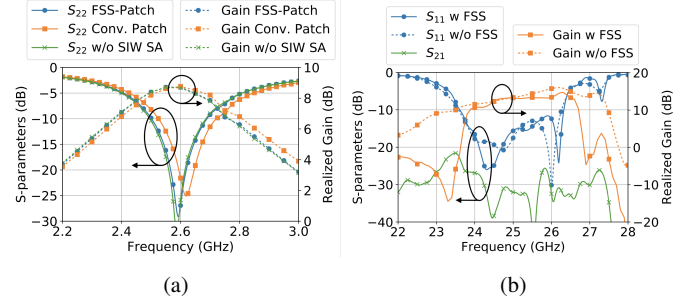

(a)   (b)

Fig. 9: Simulated S-parameters and realized gain at broadside (+z) direction at different frequencies. (a) 2.6 GHz. (b) 25 GHz.
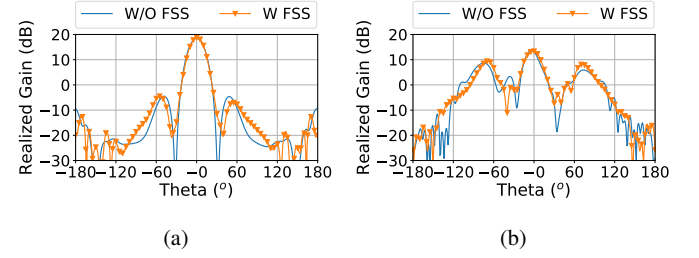

(a)   (b)

Fig. 10: E-plane radiation patterns of the K-band array at 25 GHz (a) with equal magnitude/phase through 16 discrete ports and (b) with the proposed SIW feeding network.

plane and H-plane of S-band, respectively. The plane $\Phi = 135^o$ and $\Phi = 45^o$ are the E-plane and H-plane of K-band, respectively. Since the feeding for each K-band element is not identical, the phase and magnitude of each element are not identical either, which leads to an increase of SLL in the E-plane. Fig.10(a) shows the E-plane patterns of the K-band array fed by 16 discrete ports with equal magnitude and phase. Fig.10(b) are the patterns with the SIW feeding network. As we can see, the SLL with or without FSS does not show too much difference in both cases but it is much higher when the feeding network is applied. The proposed K-band array can be replaced by a low sidelobe array according to the practical requirements and the FSS will not deteriorate the SLL.

IV. MEASUREMENTS AND RESULTS

The photograph of the fabricated dual-band SRA is shown in Fig.11. The FSS is fixed by supporting posts on the four corners of the PCB. The inner conductor of Port 2 is soldered on the top of the FSS. The S-parameters are measured with a network analyzer. The radiation patterns are measured in the anechoic chambers with near-field and far-field measuring systems at S- and K-band, respectively.

Fig.12(a) shows the simulated and measured S-parameters and realized gain at S-band. The measured S_{11} is below -10 dB from 2.48 GHz to 2.66 GHz and the relative bandwidth is 7%. Comparing to the simulation, the measured impedance matching band shifts a little lower. The realized gain is measured and simulated from 2.55 GHz to 2.65 GHz, which ranges from 8.3 dBi to 8.7 dBi in the simulation and from 7.47 dBi to 8.41 dBi in the measurement. The peak value of the gain appears at 2.55 GHz in both simulation and measurement.

Fig.12(b) shows the simulated and measured S-parameters and realized gain at K-band. The impedance matching band in the measurement is from 23.4 GHz to 26.1 GHz with the relative bandwidth of 10.9%, which slightly shifts lower comparing with the simulation. The mutual coupling between the S-band and K-band ports is lower

same -10-dB impedance matching band with or without FSS, which is from 23.6 GHz to 26.3 GHz. The relative bandwidth is 10.8%. The coupling S_{21} is below -25 dB over the operating band. The realized gain of the slot array without FSS ranges from 11.5 dBi to 16.2 dBi in the operating band from 24 GHz to 26.3 GHz and with FSS ranges from 10.7 dBi to 14.8 dBi in the same frequency band. The largest gain difference within the operating band is 2 dB at 26 GHz. It is higher than the insertion loss of the FSS at this frequency because the sidelobe level (SLL) at 26 GHz is slightly increased compared with the case without FSS. For the antenna without FSS, the realized gain has a slow decay outside the operating band. When the FSS is applied, two deep gain suppression points are observed at 23.3 GHz and 26.9 GHz. The realized gain is 10 dB lower with FSS in the band below 23.6 GHz and above 26.8 GHz.

Since the polarization of the patch antenna and the slot array has a 45° difference, the E-plane and H-plane of the S- and K-band antennas are different. The plane $\Phi = 0^o$ and $\Phi = 90^o$ are the E-
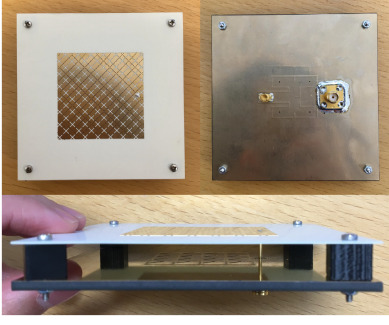
Fig. 11: Photograph of the fabricated dual-band structure reused antenna.

(a)

(b)
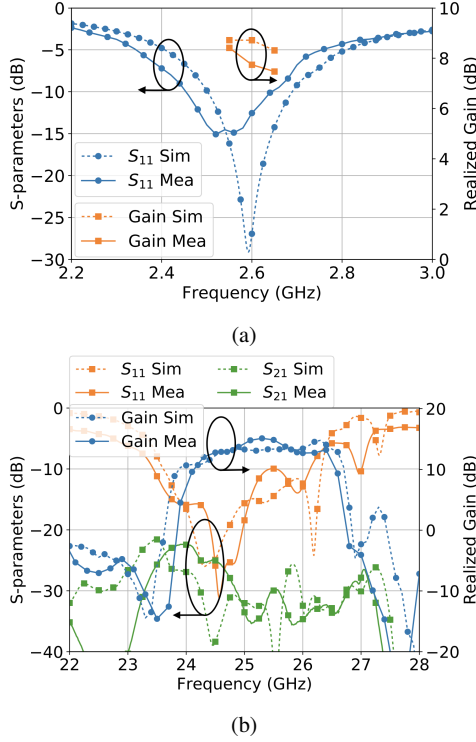
Fig. 12: Measured S-parameters and realized gain at different frequencies. (a) S-band. (b) K-band.
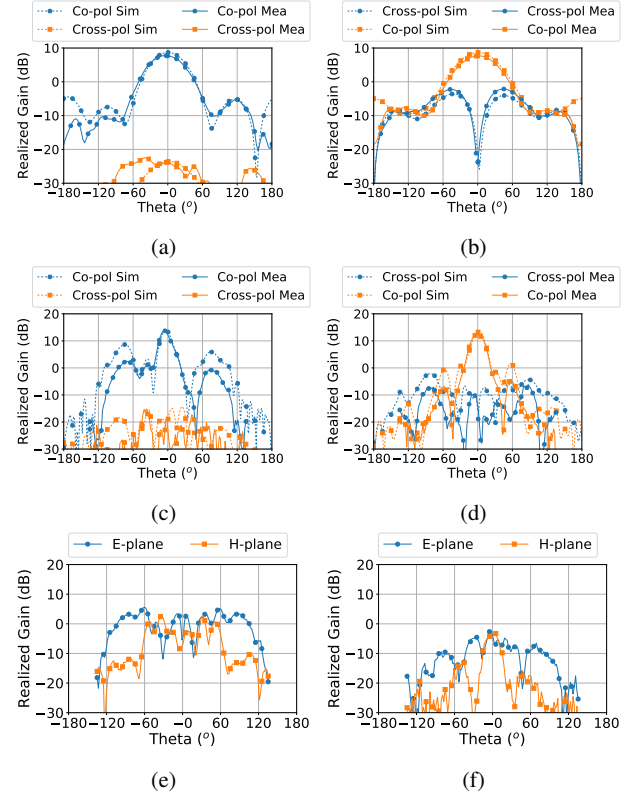

Fig. 13: Simulated and measured radiation patterns at different frequencies. (a) E-plane at 2.6 GHz. (b) H-plane at 2.6 GHz. (c) E-plane at 25 GHz. (d) H-plane at 25 GHz. (e) E-/H-plane co-polarization patterns at 23 GHz. (f) E-/H-plane co-polarization patterns at 27 GHz.
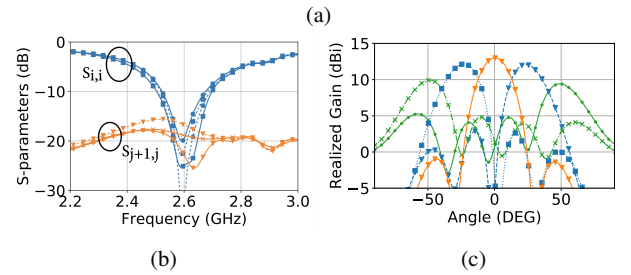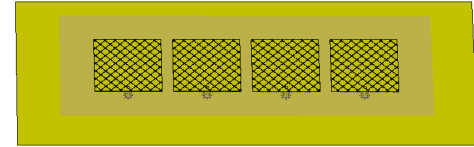

Fig. 14: Simulated 4-element MIMO array with the proposed antenna as array element. (a) Schematic of the MIMO array. (b) Reflection coefficients $S_{i,i}$, i = 1, 2, 3, 4. and mutual coupling $S_{j+1,j}$, j = 1, 2, 3. (c) Beam scanning patterns at 2.6 GHz

than -22 dB at K-band. The simulated and measured realized gain has reached a very closed value in the passband, just the measured realized gain has slightly narrower bandwidth.

The simulated and measured radiation patterns at 2.6 GHz and 25 GHz are shown in Fig.13(a)-(d). The measurements match well with the simulations. The realized gain at 2.6 GHz is 8.7 dBi and 7.7 dBi in the simulation and measurement, respectively. The measured gain is lower due to the frequency shift. The realized gain at 25 GHz is 13.8 dBi and 13.7 dBi in the simulation and measurement, respectively. Both frequencies have cross-polarization -20 dB lower than co-polarization in the broadside (+z) direction. The measured patterns in Fig.13(c) and Fig.13(d) have lower SLL than the simulated patterns. It is due to the possible frequency shift and missing the peak value of the sidelobe in the measuring plane. Fig.13(e) and (f) present the simulated and measured E- and H-plane co-polarization patterns at 23 GHz and 27 GHz, which are outside the operation band. As we can see, the radiation outside the operating band is evenly scattered by the FSS.

The proposed SRA can be used in the 5G beam steering array or Multiple-Input and Multiple-Output (MIMO) array system as one array element. Fig.14(a) shows one example of a 4-element MIMO array structure with the proposed SRA as an array element. The S-band and K-band antennas can work as two different arrays, where the S-band antennas can work as a beam steering array or a MIMO array. Fig.14(b) shows the reflection coefficients of the four array elements working at S-band and the mutual coupling between the two adjacent

TABLE II
COMPARISON WITH OTHER DUAL-BAND HIGH FR SAA

Ref No.	Operating Band (GHz) & FR	Bandwidth	Peak Gain (dBi)	RAR	SLL (dB)	Filter
[9]	5.8/60, 10.3	Not given	4/7	≈ 0	NG	No
[8]	0.45/2.2, 4.9	33.3%/15.9%	6.3/7.2	30%	NG	No
[7]	2.4/24, 10	7.3%/2.23%	7.3/11.5	≈ 0	-15	No
[10]	5.8/30, 5.2	3.1%/8.1%	10.2/8	5.6%	-2	No
[11]	3.5/60, 17	2.6%/6.4%	7.3/24	77%	-12	No
This work	2.6/25, 9.6	7%/7.6%	8/16	50%	-5	Yes

FR*: frequency ratio. RAR*: ratio of aperture reuse. SLL*: sidelobe level.

elements. The array elements have good impedance matching at 2.6 GHz and the mutual coupling is lower than -15 dB. Fig.14(c) shows the beam steering patterns at 2.6 GHz, where the scanning angle is from -50° to 50° and the realized gain ranges from 9.7 dBi to 13 dBi. The K-band array can be seen as one sub-array in a larger MIMO array. The higher gain of the K-band array compensates the higher fading of the mm-wave propagation.

Table II reports a comparison of the proposed antenna against a comprehensive set of the other dual-band high FR SAAs. The RAR, introduced in [11], is defined as the ratio between the occupied areas of the smaller and the larger radiating structures. In contrast to all the other approaches, the proposed antenna is enriched with the filtering feature, which improves the suppression of the out-of-band emission at K-band. Furthermore, the proposed antenna provides a very good trade-off between the bandwidth and the RAR compared e.g. to [8], which has better bandwidth but poor RAR, or to [11], which has better RAR but poor bandwidth. In general, the proposed approach clearly outperforms [7]–[10] in terms of RAR and outperforms [7], [10], [11] in terms of bandwidth. As explained in Section III, the proposed design shows a higher SLL compared with the other approaches. However, we stress the fact that the high SLL is the effect of the simplified feeding network. The SLL can be further reduced in practice by utilizing distributed feeding networks, which have gain control for each element. Since the radiation of the two bands can be designed individually, the RAR of the proposed antenna can be further increased by applying a larger K-band array. As a consequence, the K-band realized gain will also increase without significant influence on the S-band radiation and the filtering feature.

V. CONCLUSION

The paper proposes a dual-band SRA with quasi-elliptic bandpass feature for 5G applications. The proposed antenna operates at 2.6/25 GHz with a high FR of 9.6. A 4×4 cavity-backed slot array works from 23.4 GHz to 26.1 GHz with a bandpass FSS above it, which is also excited as a low frequency radiator working from 2.48 GHz to 2.66 GHz. Due to the asymmetric boundary of each unit cell, the proposed FSS broadens the bandwidth and achieves a good frequency selectivity with two transmission zeros in the lower and higher stopband. The FSS also has a simple structure and can be fabricated with one layer substrate. The simulations and measurements have a good matching. The proposed antenna will be a good candidate for the upcoming dual-band high FR 5G applications.

REFERENCES

[1] C. Mao, S. Gao, Y. Wang, Q. Chu, and X. Yang, "Dual-band circularly polarized shared-aperture array for c -/ x -band satellite communications," *IEEE Transactions on Antennas and Propagation*, vol. 65, no. 10, pp. 5171–5178, Oct 2017.
[2] C. Mao, S. Gao, Q. Luo, T. Rommel, and Q. Chu, "Low-cost x/ku/ka-band dual-polarized array with shared aperture," *IEEE Transactions on Antennas and Propagation*, vol. 65, no. 7, pp. 3520–3527, July 2017.
[3] K. Li, T. Dong, and Z. Xia, "A broadband shared-aperture l/s/x-band dual-polarized antenna for sar applications," *IEEE Access*, vol. 7, pp. 51 417–51 425, 2019.
[4] M. Ferrando-Rocher, J. I. Herranz-Herruzo, A. Valero-Nogueira, and B. Bernardo-Clemente, "Full-metal k-ka dual-band shared-aperture array antenna fed by combined ridge-groove gap waveguide," *IEEE Antennas and Wireless Propagation Letters*, vol. 18, no. 7, pp. 1463–1467, July 2019.
[5] K. Wang, X. Liang, W. Zhu, J. Geng, J. Li, Z. Ding, and R. Jin, "A dual-wideband dual-polarized aperture-shared patch antenna with high isolation," *IEEE Antennas and Wireless Propagation Letters*, vol. 17, no. 5, pp. 735–738, May 2018.
[6] A. B. Smolders, R. M. C. Mestrom, A. C. F. Reniers, and M. Geurts, "A shared aperture dual-frequency circularly polarized microstrip array antenna," *IEEE Antennas and Wireless Propagation Letters*, vol. 12, pp. 120–123, 2013.
[7] L. Y. Feng and K. W. Leung, "Dual-frequency folded-parallel-plate antenna with large frequency ratio," *IEEE Transactions on Antennas and Propagation*, vol. 64, no. 1, pp. 340–345, Jan 2016.
[8] F. Shen, C. Yin, K. Guo, S. Wang, Y. Gong, and Z. Guo, "Low-cost dual-band multipolarization aperture-shared antenna with single-layer substrate," *IEEE Antennas and Wireless Propagation Letters*, vol. 18, no. 7, pp. 1337–1341, July 2019.
[9] D. Wang and C. H. Chan, "Multiband antenna for wifi and wigig communications," *IEEE Antennas and Wireless Propagation Letters*, vol. 15, pp. 309–312, 2016.
[10] B. J. Xiang, S. Y. Zheng, H. Wong, Y. M. Pan, K. X. Wang, and M. H. Xia, "A flexible dual-band antenna with large frequency ratio and different radiation properties over the two bands," *IEEE Transactions on Antennas and Propagation*, vol. 66, no. 2, pp. 657–667, Feb 2018.
[11] J. F. Zhang, Y. J. Cheng, Y. R. Ding, and C. X. Bai, "A dual-band shared-aperture antenna with large frequency ratio, high aperture reuse efficiency, and high channel isolation," *IEEE Transactions on Antennas and Propagation*, vol. 67, no. 2, pp. 853–860, Feb 2019.
[12] K. Tao, B. Li, Y. Tang, M. Zhang, and Y. Bo, "Analysis and implementation of 3d bandpass frequency selective structure with high frequency selectivity," *Electronics Letters*, vol. 53, no. 5, pp. 324–326, 2017.
[13] Z. Zhao, A. Zhang, X. Chen, G. Peng, J. Li, H. Shi, and A. A. Kishk, "Bandpass fss with zeros adjustable quasi-elliptic response," *IEEE Antennas and Wireless Propagation Letters*, vol. 18, no. 6, pp. 1184–1188, June 2019.
[14] A. K. Rashid, Z. Shen, and B. Li, "An elliptical bandpass frequency selective structure based on microstrip lines," *IEEE Transactions on Antennas and Propagation*, vol. 60, no. 10, pp. 4661–4669, Oct 2012.
[15] V. Krushna Kanth and S. Raghavan, "Em design and analysis of frequency selective surface based on substrate-integrated waveguide technology for airborne radome application," *IEEE Transactions on Microwave Theory and Techniques*, vol. 67, no. 5, pp. 1727–1739, May 2019.
[16] D. S. Wang, B. J. Chen, and C. H. Chan, "High-selectivity bandpass frequency-selective surface in terahertz band," *IEEE Transactions on Terahertz Science and Technology*, vol. 6, no. 2, pp. 284–291, March 2016.
[17] G. Q. Luo, W. Hong, Q. H. Lai, K. Wu, and L. L. Sun, "Design and experimental verification of compact frequency-selective surface with quasi-elliptic bandpass response," *IEEE Transactions on Microwave Theory and Techniques*, vol. 55, no. 12, pp. 2481–2487, Dec 2007.
[18] D. Guan, Z. Qian, Y. Zhang, and J. Jin, "High-gain siw cavity-backed array antenna with wideband and low sidelobe characteristics," *IEEE Antennas and Wireless Propagation Letters*, vol. 14, pp. 1774–1777, 2015.